for microwave-based welding not found in the conducting polymers (*30*). This microwave heating process could be used to make polymer composites from stacks of polymer sheets that are separated by nanotube sheets, car windows that are electrically heated, or antennas in car windows that have high transparency.

The work function of these transparent MWNT sheets (~5.2 eV) is slightly higher than that of the ITO typically used as the transparent hole-injecting electrode in organic light-emitting diodes (OLEDs), and these sheets have the additional benefits of being porous and flexible. MWNT sheets made with previous techniques have not been successfully used for optically transmissive, hole-injecting layers in OLEDs: The sheet thickness and surface roughness dwarf the typical 100-nm layer thickness of emissive layers needed for OLEDs (*31*), thereby causing interelectrode shorts; and in thicker devices, the unbalanced hole and electron currents prevent light emission. However, black sheets of solution-spun MWNTs have been used as nontransmissive hole-collecting electrodes in solar cells (*10*), and transparent p-type SWNT sheets have been used as hole-injection electrodes in inorganic LEDs based on gallium nitride (*32*).

We have taken advantage of the nanometer-scale thickness, transparency, flexibility, porosity, and high work function of our densified MWNT sheets to demonstrate polymer-based OLEDs on both flexible plastic and rigid glass substrates (*14*). Hole injection occurs over the high-surface-area interior of the nanoporous nanotube electrode, as opposed to at a planar interface in the previous inorganic LEDs (*32*). The onset voltage for emission is quite low (2.4 V, about the same as for the highest-performance ITO in similar devices), and rather bright electroluminescence was obtained (up to 500 cd/m^2) (fig. S7). The emitted light is slightly polarized, but in an orthogonal direction from that for the above incandescent light source, because the MWNT sheet acts as a polarizer. If a polymeric light-emitting layer were aligned using known methods (*33*) to provide emission in the same polarization direction, absorption due to the MWNT hole injector could be minimized, which is not possible for conventional ITO hole-injecting electrodes.

Although solution- or melt-based processing becomes increasingly difficult as nanofiber length increases, the opposite is true for the present solid-state sheet fabrication process: 300-μm-long nanotubes are easier to convert into sheets than are 70-μm-long nanotubes. Also, ultrasonication used for nanotube dispersion in solution-based processing decreases nanotube length, and this degradative step is absent from the present sheet fabrication process. These are important advantages of the present technology, because long, high-perfection nanotubes are needed for maximizing electrical and thermal conductivities and mechanical properties.

References and Notes

1. A. G. Rinzler *et al.*, *Appl. Phys. A* **67**, 29 (1998).
2. M. Endo *et al.*, *Nature* **433**, 476 (2005).
3. Z. Wu *et al.*, *Science* **305**, 1273 (2004).
4. L. Hu, D. S. Hecht, G. Grüner, *Nano Lett.* **4**, 2513 (2004).
5. J. E. Fischer *et al.*, *J. Appl. Phys.* **93**, 2157 (2003).
6. W. A. De Heer *et al.*, *Science* **268**, 845 (1995).
7. Y. Li, I. A. Kinloch, A. H. Windle, *Science* **304**, 276 (2004).
8. Y. Kim *et al.*, *Jpn. J. Appl. Phys.* **42**, 7629 (2003).
9. T. V. Sreekumar *et al.*, *Chem. Mater.* **15**, 175 (2003).
10. H. Ago, K. Petritsch, M. S. P. Shaffer, A. H. Windle, R. H. Friend, *Adv. Mater.* **11**, 1281 (1999).
11. K. Jiang, Q. Li, S. Fan, *Nature* **419**, 801 (2002).
12. M. Zhang, K. R. Atkinson, R. H. Baughman, *Science* **306**, 1358 (2004).
13. The per-sheet thickness measured by stylus profilometer varied from ~50 to ~150 nm, depending on forest height and draw and densification conditions. Atomic force microscopy provides a sheet thickness of down to 30 to 50 nm, which is close to the maximum width of fibrils in the sheet, which can be far from cylindrical.
14. See supporting data on *Science* Online.
15. P. G. Collins, M. S. Fuhrer, A. Zettl, *Appl. Phys. Lett.* **76**, 894 (2000).
16. H. Ouacha *et al.*, *Appl. Phys. Lett.* **80**, 1055 (2002).
17. L. Roschier, R. Tarkiainen, M. Ahlskog, M. Paalanen, P. Hakonen, *Appl. Phys. Lett.* **78**, 3295 (2001).
18. A 1-mm-thick sheet of silicone rubber (ECOFLEX 0040 from Smooth-On) was stretched to 105% strain, and then a single as-drawn MWNT sheet was laid over it to provide self-generated adhesive contact before strain relaxation. The initial sheet resistance of the obtained unloaded silicone rubber/MWNT sheet composite was 755 ohms per square. However, after an initial increase in resistance by ~6%, the resistance changed less than 3% during the subsequent four strain cycles to 100% strain.
19. R. Pelrine, R. Kornbluh, Q. Pei, J. Joseph, *Science* **287**, 836 (2000).
20. K. Hata *et al.*, *Science* **306**, 1362 (2004).
21. D. E. Edwards *et al.*, *High Perf. Polymers* **16**, 277 (2004).
22. L. M. Ericson *et al.*, *Science* **305**, 1447 (2004).
23. M. E. Kozlov *et al.*, *Adv. Mater.* **17**, 614 (2005).
24. J. N. Coleman *et al.*, *Appl. Phys. Lett.* **82**, 1682 (2003).
25. B. Vigolo, P. Poulin, M. Lucas, P. Launois, P. Bernier, *Appl. Phys. Lett.* **81**, 1210 (2002).
26. A. B. Dalton *et al.*, *Nature* **423**, 703 (2003).
27. P. Li *et al.*, *Appl. Phys. Lett.* **82**, 1763 (2003).
28. P. C. P. Watts, W.-K. Hsu, A. Barnes, B. Chambers, *Adv. Mater.* **15**, 600 (2003).
29. J. Wu, L. Kong, *Appl. Phys. Lett.* **84**, 4956 (2004).
30. A. J. Epstein, A. G. MacDiarmid, *Synth. Metals* **69**, 179 (1995).
31. D. B. Romero, M. Carrard, W. De Heer, L. Zuppiroli, *Adv. Mater.* **8**, 899 (1996).
32. K. Lee, Z. Wu, Z. Chen, F. Ren, S. J. Pearton, A. G. Rinzler, *Nano Lett.* **4**, 911 (2004).
33. K. S. Whitehead, M. Grell, D. D. C. Bradley, M. Jandke, P. Strohriegl, *Appl. Phys. Lett.* **76**, 2946 (2000).

34. Supported by Defense Advanced Research Projects Agency/U.S. Army Research Office grant W911NF-04-1-0174, the Texas Advanced Technology Program grant 009741-0130-2003, the Air Force STTR program on topic AF04-TO20, Air Force grant F49620-03-1-0164, Robert A. Welch Foundation grant AT-0029, and the Strategic Partnership for Research in Nanotechnology consortium in Texas. The authors thank J. P. Ferraris and M. Zhou for the synthesis of the emissive polymer used for the OLEDs, A. Kuznetsov for assistance with OLED preparation, and V. H. Ebron for assistance with the microwave welding.

Supporting Online Material

www.sciencemag.org/cgi/content/full/309/5738/1215/DC1
Materials and Methods
Figs. S1 to S7
References
Movies S1 and S2

25 May 2005; accepted 13 July 2005
10.1126/science.1115311

Understanding the Infrared Spectrum of Bare CH_5^+

Oskar Asvany,[1]* Padma Kumar P,[2]* Britta Redlich,[3] Ilka Hegemann,[2] Stephan Schlemmer,[1,4] Dominik Marx[2]†

Protonated methane, CH_5^+, continues to elude definitive structural assignment, as large-amplitude vibrations and hydrogen scrambling challenge both theory and experiment. Here, the infrared spectrum of bare CH_5^+ is presented, as detected by reaction with carbon dioxide gas after resonant excitation by the free electron laser at the FELIX facility in the Netherlands. Comparison of the experimental spectrum at ~110 kelvin to finite-temperature infrared spectra, calculated by ab initio molecular dynamics, supports fluxionality of bare CH_5^+ under experimental conditions and provides a dynamical mechanism for exchange of hydrogens between CH_3 tripod positions and the three-center bonded H_2 moiety, which eventually leads to full hydrogen scrambling. The possibility of artificially freezing out scrambling and internal rotation in the simulations allowed assignment of the infrared spectrum despite this pronounced fluxionality.

Protonated methane, CH_5^+, is of great interest in vibrational spectroscopy (*1–4*) as the prototype of hypercoordinated carbon and three-center two-electron bonding (*5*, *6*). The equilibrium structure—that is, the global minimum of its potential energy surface (PES)—can be viewed as a CH_3 tripod with a H_2 moiety attached to the carbon in an eclipsed C_s configuration, e-C_s, via a three-center bond (*7*). However, rapid hydrogen scrambling has called into question the notion of assigning it such a traditional molecular structure (*8–11*), despite the stability of CH_5^+ once it is formed (*12*). This fluxionality has been traced back

to an unusually shallow PES (*13*–*15*). A staggered structure, s-C_s, only ~0.1 kcal/mol higher in energy (*15*) than e-C_s, is reached by internal rotation of the H_2 moiety about the quasi-C_3 axis while keeping the three-center bonding pattern. Most important, a structure where the H_2 moiety is broken apart—a C_{2v} first-order saddle point characterized by four-center four-electron bonding (*7*)—is only ~0.8 kcal/mol (corresponding to ~300 cm^{-1} or 0.03 eV) above the e-C_s ground state (*15*). This allows for large-amplitude motion upon quantum mechanical and/or thermal rotational-vibrational excitation (*16*–*23*).

Without direct access to real-space structure and dynamics (*24*), the only link between experiment and theory to date has been spectroscopy. After considerable experimental effort (*1*, *2*), including a pioneering infrared (IR) study (*3*) of the microsolvated cation $CH_5^+ \cdot (H_2)_{n\geq 1}$, the high-frequency wing of the C-H stretching band of bare CH_5^+ was recently published (*4*). However, no assignment or even qualitative understanding could be offered (*4*); hence, clear evidence of fluxionality, challenged by mass spectrometric data (*25*, *26*), is still lacking. On the other hand, given a molecule that continuously changes not only its shape and the symmetry of its instantaneous structure but also its chemical bonding topology through rapid intramolecular dynamics, it is unclear how the IR spectrum would look or how such a spectrum could be assigned once known.

Here, the IR spectrum of bare, cold CH_5^+ could be studied by combining a low-temperature 22-pole ion trap with the large tuning range of the free electron laser (FEL) at the FELIX facility (*27*, *28*) and the laser-induced reaction (LIR) technique. In LIR, infrared excitation induces a bimolecular reaction of the parent molecule, CH_5^+, and the amount of product formed is a measure of the absorption intensity as a function of the excitation wavelength. The major benefits of LIR are the storage of mass-selected ions at variable temperatures, 10 to 300 K, in conjunction with mass analysis of product ions that are detected with close to perfect efficiency. Thus, LIR can be much more sensitive than traditional absorption detection techniques. The experimental spectra are complemented by the calculation of anharmonic IR spectra via ab initio molecular dynamics (*29*–*31*). Dissecting the trajectories obtained in full dimensionality elucidates the scrambling mechanism and its effect on the spectrum. Furthermore, comparison of the computed and the measured stretching and bending modes strongly supports fluxionality of bare CH_5^+ under experimental conditions. Most notably, the computational strategy of artificially freezing out scrambling and internal rotation paves the way for assigning the IR spectrum.

In the experiment, mass-selected ions are stored in a variable-temperature 22-pole ion trap (Fig. 1). In the trap they interact with reactant gas of constant number density and with the radiation field of an IR laser held at a constant wavelength. After a trapping time of several seconds, reactant and product ions are extracted, mass-analyzed, and detected with near-100% collection efficiency. An action spectrum of the parent ion is obtained by recording the number of mass-selected product ions as a function of the IR wavelength. In previous LIR benchmarks (*32*–*34*), a small endothermicity hindered the reaction of interest but was overcome by the resonant excitation of the parent ion. For the spectroscopy of CH_5^+, the endothermic proton transfer reaction $CH_5^+ + CO_2 \xrightarrow{h\nu} CH_4 + OCOH^+$ was chosen (*35*). The difference in proton affinities of CO_2 and CH_4 amounts to an endothermicity of ~0.7 kcal/mol ≈ 250 cm^{-1}, implying that the reaction proceeds very slowly at the trap temperature of 110 (±5) K. With each filling of the 22-pole trap, an ensemble of about 3000 CH_5^+ ions was stored for 4 s in the cold CO_2 gas environment and exposed to the tunable IR light of the FELIX FEL (*27*, *28*). After this storage period, the number of $OCOH^+$ ions produced by LIR was recorded, the laser was tuned to the next frequency, and the trap was filled again. The FEL was operated at its maximum repetition rate of 10 Hz with pulses having a typical length of 7 μs and an energy content varying from 10 to 30 mJ (at user station) depending on the wavelength region. The bandwidth of the FELIX FEL is adjustable but always transform-limited; here, the resolution was set to ~0.5% full width at half maximum of the central frequency at a given wavelength.

The product ion counts were background-corrected and divided by the spectral energy density $\rho = P/(A \cdot c \cdot \Delta\nu)$, where P, A, and $\Delta\nu$ are the power, area, and bandwidth of the laser beam, respectively, and c is speed of light. The resulting normalized action spectrum corresponds to the product of the Einstein $B(\nu)$ coefficient, the population g of the accessible rotational states, and the reaction probability of the excited CH_5^+ with neutral CO_2 gas (*35*). To a first approximation, this reaction probability is proportional to the rate coefficient $k^*(\nu)$ of the excited ion, which, unfortunately, is unknown. Because of the limited resolution of the laser, $\Delta\nu \propto \nu$, an increasing number of rotational states is excited simultaneously with increasing photon energy, $h\nu$. Assuming a linear relationship between g and the laser bandwidth, $g \sim \Delta\nu \sim \nu$, the LIR signal should be proportional to the product of the absorption cross section $\alpha(\nu)$ and $k^*(\nu)$.

The resulting experimental spectrum (Fig. 2A) consists of a very broad high-frequency band extending from about 2200 cm^{-1} beyond 3200 cm^{-1}; only the dominant peak close to 3000 cm^{-1} was observed earlier (*3*, *4*). The frequency range probed here reveals important additional features: Substructures extending down to about 2200 cm^{-1} are discernible at the low-frequency wing of the dominant C-H stretching peak. Furthermore, a broad and featureless unimodal bending band is found near 1250 cm^{-1}. Note that the reaction probability

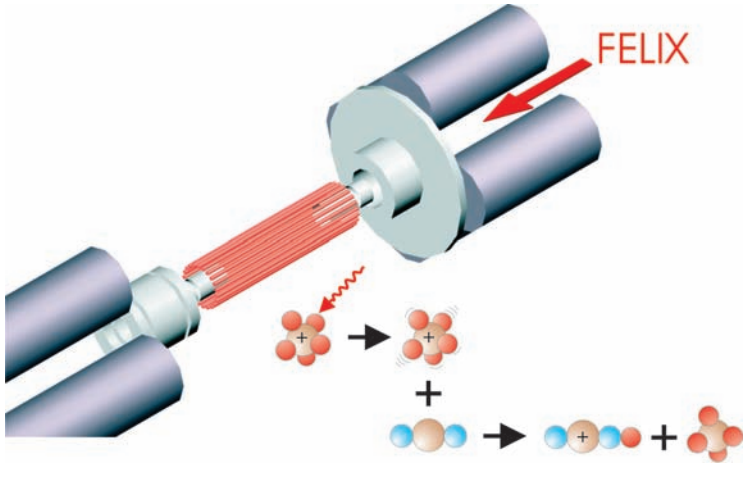

Fig. 1. Schematic of the 22-pole ion trap as used for LIR. The mass-selected ensemble of ions is injected into the trap from the left and kept there for several seconds. Once captured, the ions are cooled down to the trap temperature (110 K) by a short, intense helium pulse. In the trap, the ions are exposed to reactant gas molecules and tunable laser light (coming from the right through the axially transparent setup). The result of this interaction is detected by extracting the stored ion cloud to the right into a mass filter and counting the number of product ions. An action spectrum of the stored parent ions is recorded by repeating this process while scanning the IR laser. Color code: orange, carbon; red, hydrogen; blue, oxygen.

[1]Leiden Observatory, 2300 RA Leiden, Netherlands. [2]Lehrstuhl für Theoretische Chemie, Ruhr-Universität Bochum, 44780 Bochum, Germany. [3]FELIX Facility, Foundation for Fundamental Research on Matter (FOM) Institute for Plasma Physics "Rijnhuizen," 3430 BE Nieuwegein, Netherlands. [4]I. Physikalisches Institut, Universität zu Köln, Zülpicher Strasse 77, 50937 Köln, Germany.

*These authors contributed equally to this work.
†To whom correspondence should be addressed. E-mail: dominik.marx@theochem.rub.de

(and thus the a priori sensitivity of the experiment) decreases with decreasing frequency, approaching the small thermal rate coefficient k observed without laser excitation [$k^*(\nu) \xrightarrow{\nu \to 0} k$; see dashed line in Fig. 2A]; thus, features at much lower frequencies are difficult to detect.

To link these experimental data to a molecular picture, we computed the IR spectrum of bare CH_5^+ at finite temperatures from the Fourier transform of the classical time-autocorrelation function of the total dipole moment, subject to a quantum correction most suitable for vibrational spectra including anharmonic floppy modes (*36*). The underlying trajectories were generated by ab initio molecular dynamics (*29*–*31*) relying on a density functional approach (*17*, *18*) well-tested for comparable benchmark structures and energies (*14*, *15*). The absorption cross sections $\alpha(\nu)$ shown in Fig. 2, B and C, denoted "high"- and "low"-temperature spectra, were obtained as a canonical average based on independent microcanonical trajectories sampled from Nosé-Hoover chain (*30*) constant-temperature runs at 300 and 50 K, respectively. The high-temperature simulations at 300 K lead to a behavior known to emulate closely the true ground-state quantum behavior (*17*, *18*), whereas at ~50 K hydrogen scrambling is frozen and the internal rotation of the H_2 moiety is partly frozen.

This freezing restriction clearly is an artifact, because it is known that the molecule scrambles even in the ground state once nuclear quantum effects are accounted for (*9*, *17*, *18*). However, at the same time, it is an extremely useful computational trick for separating the impact of hydrogen scrambling and internal rotation from trivial effects due to small-amplitude motion. Thus, the "low-temperature" spectrum is not the expected experimental one for bare CH_5^+ at that temperature, but rather is a simplification for understanding the spectral features of the computed "high-temperature" spectrum, which in turn should approximate the measured one. In addition, standard power spectra or vibrational densities of states (VDOS), based on suitably defined velocity autocorrelation functions of (quasi-) local modes, are of great help in assigning the spectrum.

Overall, the computed spectrum depicted (Fig. 2B) compares favorably with experiment (Fig. 2A). In particular, there are three subpeaks contributing to the broad band extending from about 2200 to 3400 cm^{-1} in addition to a rather symmetric peak close to 1200 cm^{-1}; note that the usual frequency scaling (*14*, *37*) by an empirical correction factor of typically 0.91 to 0.95 would yield quantitative agreement. Generally, the corresponding VDOS above and below 2000 cm^{-1} can by approximation be decoupled upon projection onto C-H stretching and H-C-H bending coordinates, respectively; the broad feature near 1200 cm^{-1}, which comprises five modes in the harmonic approximation (*14*, *19*), is close to the highly degenerate bending mode of CH_4. Further decomposition of the high-temperature spectrum (Fig. 2B) is hampered by the fact that the instantaneous arrangement of atoms (i.e., the molecular structure) is constantly changing as a result of hydrogen scrambling (*23*).

Fortunately, the artificial cooling of the molecule to a sufficiently low temperature results in freezing of the scrambling dynamics. In this nonscrambling regime (Fig. 2C), the most prominent peak splits into a triplet centered near 3220 cm^{-1}, which is close to both the experimental and calculated (≈ 3210 cm^{-1}) C-H stretching frequency of CH_4; we also note the good agreement of the low-temperature IR peak positions in Fig. 2C with the resonances of the low-energy power spectrum (*19*) obtained from a PES at the MP2/cc-pVTZ level of theory. Most interesting, however, is the qualitative agreement of the triplet structure (due to tripod stretching modes; see below) observed only in the nonscrambling regime with the emergence of a three-peak characteristic in the measured IR spectrum (*3*) under progressive microsolvation of bare CH_5^+ by H_2, which has been interpreted as being caused by a slowing down of the scrambling dynamics.

Extended time intervals exist in the nonscrambling regime where the internal rotation of the H_2 moiety about the pseudo-C_3 axis is either free or hindered. In the latter so-called librational regime, only librational motion in the e-C_s minimum is possible, whereas in the former (rotational) regime, full rotation is activated, thus interconverting the e-C_s and s-C_s structures (Fig. 3). Decomposition of the VDOS reveals that the central peak of the triplet gains intensity in the rotational regime, where all three tripod hydrogens are statistically equivalent. This dynamical degeneracy, however, is lifted in the librational regime, which favors the eclipsed equilibrium structure, e-C_s, and results in red- and blue-shifted satellites. The central peak and its blue-shifted satellite are respectively assigned to symmetric and antisymmetric stretches of the tripod hydrogens that are instantaneously non-eclipsed by the H_2 moiety, whereas the red-shifted satellite is due to stretching of the eclipsed tripod hydrogen (*14*). Despite the observed pronounced mixing of stretching and bending modes due to anharmonicity, the peak doublet around 2425 and 2700 cm^{-1}, which is a well-separated feature only in the nonscrambling regime, can approximately be assigned to those antisymmetric and symmetric stretching modes that involve only the H_2 moiety in agreement with the harmonic analysis (*14*).

Thus, the protons forming the H_2 moiety and those engaged in the CH_3 tripod lead to three well-separated stretching peaks in the low-temperature regime, the prominent one of highest frequency (tripod modes) having a triplet substructure. In the high-temperature regime where the computed spectrum matches closely the experimental one, the lifetime of the H_2 moiety is ~55 fs, allowing for several C-H stretching vibrational periods in C_s-like structures. In comparison, the time spent close to the transition state for scrambling (see below), corresponding to the lifetime of C_{2v}-like structures, is considerably shorter: ~10 fs. Thus, the three-center two-electron bonding pattern, characterizing the C_s-like ground-state structure and the resulting correlated motion of the five protons around the central carbon

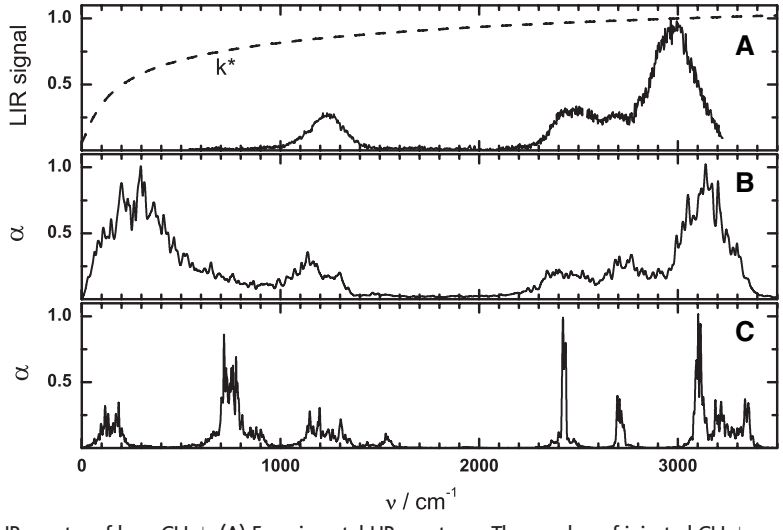

Fig. 2. IR spectra of bare CH_5^+. (**A**) Experimental LIR spectrum. The number of injected CH_5^+ parent ions is >3000, the $OCOH^+$ signal ion count had a maximum of ~500 at the C-H bend frequency (1250 cm^{-1}), and the data were normalized as described in the text. The LIR rate coefficient $k^*(\nu)/k^*$(3000 cm^{-1}), shown by dashed line, was calculated on the basis of the heat capacity of CH_5^+, the temperature of the experiment (110 K), and the endothermicity of the LIR reaction (*35*). (**B** and **C**) Absorption cross sections from high-temperature (B) and low-temperature (C) ab initio simulations; see text for details.

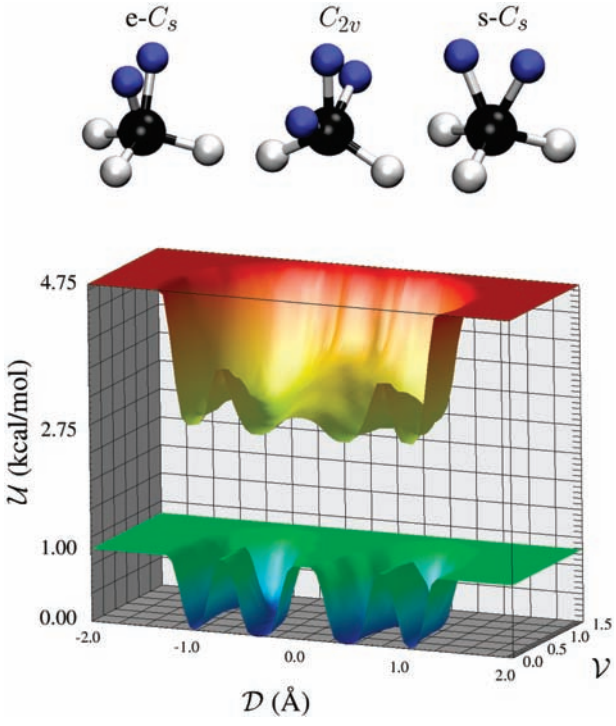

Fig. 3. Top: Eclipsed (e-C_s) and staggered (s-C_s) structures with CH_3 tripod (black and gray) and H_2 moiety (blue); saddle point structure (C_{2v}) with three coplanar hydrogen atoms (blue). Bottom: Effective PES $\mathcal{U}$ as a function of the generalized coordinates $\mathcal{D}$ and $\mathcal{V}$ (see text), shown at high (upper graph) and low (lower graph) temperature, corresponding to the scrambling (*23*) and nonscrambling regime, respectively. For the purpose of presentation, $\mathcal{U}(\mathcal{D},\mathcal{V})$ is smoothed and set to a constant value above 4.75 kcal/mol in the upper graph and 1.00 kcal/mol in the lower graph.

nucleus, is the key to understanding the IR spectrum, despite the underlying scrambling dynamics.

Having identified hydrogen scrambling as the dominant dynamical process, the underlying rearrangement path can be analyzed with the help of Fig. 3. An effective PES, $\mathcal{U}$, as explored by the two sets of simulations, is shown in a subspace spanned by $\mathcal{D} = \pm|d_{12} - d_{23}|$ (where d_{ij} is the distance between $H^{(i)}$ and $H^{(j)}$) and $\mathcal{V} = \hat{\mathbf{n}}_{1,2}\cdot\hat{\mathbf{r}}_3$ (where $\hat{\mathbf{n}}_{1,2}$ is the unit normal to the plane containing $\hat{\mathbf{r}}_1$ and $\hat{\mathbf{r}}_2$, and $\hat{\mathbf{r}}_i$ denote the unit vectors along the C-$H^{(i)}$ bonds) averaged over the fluctuations in all remaining degrees of freedom. The three protons $H^{(1)}$, $H^{(2)}$, and $H^{(3)}$ are those that are instantaneously involved in hydrogen scrambling events, as identified before and after every such event by analyzing the configurational trajectories. Briefly, $\mathcal{V}$ measures deviations of the three scrambling protons from coplanarity (where $\mathcal{V} = 0$), whereas $\mathcal{D}$ is sensitive to their deviations from the C_{2v} saddle point arrangement (where $\mathcal{D} = 0$). In the low-temperature limit of artificially frozen hydrogen scrambling (lower graph in Fig. 3), only internal rotational motion of the H_2 moiety is possible, interconverting the e-C_s and s-C_s structures without breaking up the H_2 moiety. This restriction leads to two steep, fully disconnected, horseshoe-like valleys, implying that the molecule never explores the PES close to $(\mathcal{D},\mathcal{V}) = (0,0)$.

Upon activating scrambling (*23*) by increasing the temperature (upper graph), the two valleys broaden and become connected by an extremely flat ridge, thus yielding an unusually shallow PES in the scrambling coordinates. In particular, the most probable connecting path passes through $(\mathcal{D},\mathcal{V}) \approx (0,0)$, which characterizes the C_{2v} first-order saddle point. Thus, this analysis of the PES topology strongly supports the idea that the C_{2v} structure can serve as a meaningful approximation to the transition complex structure for the scrambling motion in CH_5^+, although deviations very large in amplitude (i.e., $\mathcal{V} \gg 0$) are observed in view of the flatness of the ridge. In the scrambling regime, the effective barrier for this process is ~0.3 kcal/mol, versus ~0.6 kcal/mol obtained along the minimum-energy path from the static e-C_s and C_{2v} structures. This low value implies that fluctuations of the remaining degrees of freedom suppress the effective barrier to hydrogen scrambling considerably, calling into question reduced-dimensionality theories.

Together, these experiments and simulations clearly indicate full hydrogen scrambling of bare CH_5^+ at experimental conditions. In addition to describing the scrambling mechanism in atomic detail, the presented methods offer an understanding of the measured IR spectrum despite the underlying rapid proton motion that dynamically interconverts structures of different symmetry and chemical bonding pattern. In particular, the fact that the C-H stretching modes of the H_2 moiety and CH_3 tripod resolve into distinct peaks is arguably an experimental support for three-center two-electron bonding being operative in bare CH_5^+ under experimental conditions. The current approach to IR spectra could guide future studies on cold molecular ions in general, exploiting the use of deuterated species, overtone spectroscopy, microsolvation, and double-resonance techniques.

References and Notes

1. R. J. Saykally, *Science* **239**, 157 (1988).
2. T. Oka, *Philos. Trans. R. Soc. London Ser. A* **324**, 81 (1988).
3. D. W. Boo, Z. F. Liu, A. G. Suits, J. S. Tse, Y. T. Lee, *Science* **269**, 57 (1995).
4. E. T. White, J. Tang, T. Oka, *Science* **284**, 135 (1999).
5. G. A. Olah, *Angew. Chem. Int. Ed. Engl.* **34**, 1393 (1995).
6. G. A. Olah, G. Rasul, *Acc. Chem. Res.* **30**, 245 (1997).
7. D. Marx, A. Savin, *Angew. Chem. Int. Ed. Engl.* **36**, 2077 (1997).
8. G. A. Scuseria, *Nature* **366**, 512 (1993).
9. D. Marx, M. Parrinello, *Science* **284**, 59 (1999).
10. P. R. Schreiner, *Angew. Chem. Int. Ed. Engl.* **39**, 3239 (2000).
11. D. Gerlich, *Phys. Chem. Chem. Phys.* **7**, 1583 (2005).
12. D. Talbi, R. P. Saxon, *Astron. Astrophys.* **261**, 671 (1992).
13. V. Dyczmons, W. Kutzelnigg, *Theor. Chim. Acta (Berlin)* **33**, 239 (1974).
14. P. R. Schreiner, S.-J. Kim, H. F. Schaefer III, P. von Ragué Schleyer, *J. Chem. Phys.* **99**, 3716 (1993).
15. H. Müller, W. Kutzelnigg, J. Noga, W. Klopper, *J. Chem. Phys.* **106**, 1863 (1997).
16. J. S. Tse, D. D. Klug, K. Laasonen, *Phys. Rev. Lett.* **74**, 876 (1995).
17. D. Marx, M. Parrinello, *Nature* **375**, 216 (1995).
18. D. Marx, M. Parrinello, *Z. Phys. D* **41**, 253 (1997).
19. A. Brown, B. J. Braams, K. Christoffel, Z. Jin, J. M. Bowman, *J. Chem. Phys.* **119**, 8790 (2003).
20. A. B. McCoy *et al.*, *J. Phys. Chem. A* **108**, 4991 (2004).
21. A. Brown, A. B. McCoy, B. J. Braams, Z. Jin, J. M. Bowman, *J. Chem. Phys.* **121**, 4105 (2004).
22. K. C. Thompson, D. L. Crittenden, M. J. T. Jordan, *J. Am. Chem. Soc.* **127**, 4954 (2005).
23. For an animation of the scrambling dynamics, see www.theochem.rub.de/go/ch5p.html.
24. D. Marx, M. Parrinello, *Science* **271**, 179 (1996).
25. A. J. R. Heck, L. J. de Koning, N. M. M. Nibbering, *J. Am. Soc. Mass Spectrom.* **2**, 453 (1991).
26. G. M. Kramer, T. Oka, E. T. White, D. Marx, M. Parrinello, *Science* **286**, 1051a (1999).
27. D. Oepts, A. F. G. van der Meer, P. W. van Amersfoort, *Infrared Phys. Technol.* **36**, 297 (1995).
28. FELIX users' page (www.rijnh.nl/felix).
29. R. Car, M. Parrinello, *Phys. Rev. Lett.* **55**, 2471 (1985).
30. D. Marx, J. Hutter, in *Modern Methods and Algorithms of Quantum Chemistry*, J. Grotendorst, Ed. [John von Neumann-Institut für Computing (NIC), Forschungszentrum Jülich, Jülich, Germany, 2000], pp. 301–449 (available at www.theochem.rub.de/go/cprev.html).
31. J. Hutter *et al.*, CPMD Software Package, Max-Planck-Institut für Festkörperforschung and IBM Zürich (1995–1999).
32. S. Schlemmer, T. Kuhn, E. Lescop, D. Gerlich, *Int. J. Mass Spectrom.* **185**, 589 (1999).
33. S. Schlemmer, E. Lescop, J. von Richthofen, D. Gerlich, M. A. Smith, *J. Chem. Phys.* **117**, 2068 (2002).
34. O. Asvany, T. Giesen, B. Redlich, S. Schlemmer, *Phys. Rev. Lett.* **94**, 073001 (2005).
35. S. Schlemmer, O. Asvany, *J. Phys. Conf. Ser.* **4**, 134 (2005).
36. R. Ramírez, T. López-Ciudad, P. Kumar P, D. Marx, *J. Chem. Phys.* **121**, 3973 (2004).
37. A. P. Scott, L. Radom, *J. Phys. Chem.* **100**, 16502 (1996).

38. Supported by Deutsche Forschungsgemeinschaft (DFG) Forschergruppe FOR 388 ("Laboratory Astrophysics") and DFG grant MA 1547/4-1, the Netherlands Research School for Astronomy (NOVA), Fonds der Chemischen Industrie, and a Netherlands Organization for Scientific Research (NWO) Spinoza grant (O.A.). The Bochum group thanks A. Chandra, H. Forbert, A. Kohlmeyer, and H. Langer for useful discussions and technical help; the simulations were carried out at BOVILAB@RUB (Bochum). The Leiden/Köln group thanks FOM for beam time and highly appreciates the skillful assistance by the FELIX staff and by the workshops of Leiden University. S.S. thanks D. Gerlich for the opportunity to transfer the 22-pole ion trap machine to Leiden/Köln in order to continue the work on LIR.

18 April 2005; accepted 22 June 2005
Published online 30 June 2005;
10.1126/science.1113729
Include this information when citing this paper.